
Article:
Rubino, P orcid.org/0000-0001-8669-6747, Keeley, J orcid.org/0000-0001-5251-6648, Sulollari, N orcid.org/0000-0003-0703-1603 et al. (9 more authors) (2021) All-electronic phase-resolved THz microscopy using the self-mixing effect in a semiconductor laser. ACS Photonics, 8 (4). pp. 1001-1006. ISSN 2330-4022

https://doi.org/10.1021/acsphotonics.0c01908

All-electronic phase-resolved THz microscopy using the self-mixing effect in a semiconductor laser

Pierluigi Rubino[1], James Keeley[1], Nikollao Sulollari[1], Andrew D. Burnett[2], Alex Valavanis[1], Imon Kundu[1], Mark C. Rosamond,[1] Lianhe Li[1], Edmund H. Linfield[1], A. Giles Davies[1], John E. Cunningham[1] and Paul Dean[1]

[1] School of Electronic and Electrical Engineering, University of Leeds, Leeds, LS2 9JT UK

[2] School of Chemistry, University of Leeds, Leeds, LS2 9JT UK

ABSTRACT: We report all-electronic coherent scattering-type scanning near-field microscopy (s-SNOM) using a terahertz-frequency quantum cascade laser. By exploiting the coherent self-mixing effect in these lasers, in conjunction with electronic frequency tuning of the laser, we demonstrate spatial mapping of both the amplitude and phase of the scattered field with deeply sub-wavelength resolution. We apply our technique for coherent microscopy of a phonon-resonant crystal. The extracted amplitude and phase parameters reveal clear contrast when compared to both metallic and non-resonant dielectric materials, and show excellent agreement with those calculated using a finite-dipole model of the near-field interaction between the s-SNOM tip and the resonant sample in the Reststrahlen band. Our technique paves the way for fast nanoscale-resolved mapping of the dielectric function of solid state systems and optoelectronic nanodevices at terahertz frequencies.

KEYWORDS: Terahertz, scattering-type Scanning Near-Field Microscopy, coherent imaging, Quantum cascade lasers, Self-mixing

Terahertz (THz) frequency radiation offers unique capabilities for studying low-energy electronic and vibrational excitations in condensed matter systems.[1,2] This has motivated the widespread uptake of THz technologies for the optical characterisation and spatio-temporal mapping of the bulk dielectric and magnetic properties of a broad range of materials including crystalline solids[1,3] semiconductors,[4–6] superconductors,[7,8] ferroelectric[9] and ferromagnetic[10] materials, and biological systems.[11,12] The energy scales associated with THz radiation have furthermore enabled the exploration of a wealth of fundamental physical phenomena in nanoscale systems and low-dimensional quantum structures,[13–15] as well as 2D materials and their combined Van der Waals heterostructures.[16–18] The optical characterisation of such systems most commonly relies on optical measurements in the far-field of the sample. However, this approach intrinsically restricts such measurements to the ensemble sampling of physical properties averaged over the diffraction-limited optical beam size, which is typically >100 μm at THz frequencies. Crucially, this hinders the study of individual nanoparticles, nanocrystals or molecules, and furthermore limits the investigation of physical phenomena occurring over sub-wavelength length scales.

In recent years there has been significant interest in the use of scattering-type scanning near-field microscopy (s-SNOM)[19,20] to overcome the diffraction limit at THz frequencies. In this scheme incident radiation is strongly confined at the nanoscale tip of an atomic force microscope probe positioned in the near-field of the sample surface. By collecting the field scattered to the far-field the local dielectric properties of the sample can be probed with deeply sub-wavelength resolution. This powerful technique has enabled a host of THz measurements on the micro- and nano-scale, including the mapping of charge carriers in semiconductors and nanostructures,[14,21,22] the microscopic investigation of quantum dots,[23] metamaterials[24] and nanoantennas,[25] and the spatial mapping of acoustic plasmons in graphene.[18]

Yet one limitation of THz-s-SNOM is the weak scattering efficiency of the tip, which scales approximately as $\sim\lambda^{-4}$ and is extremely low at THz frequencies. One means to address this issue is to employ a high power THz quantum cascade laser (QCL) source coupled with the high detection sensitivity afforded by laser feedback interferometry (LFI) based on the self-mixing (SM) effect in these lasers.[26] In addition to remarkably low noise-equivalent powers at the ~pW/√Hz level,[27] the LFI scheme offers the capability of sensing weak scattered fields via the laser voltage, without the need for any external detector. Moreover, the coherent mixing process between reinjected and laser cavity fields in the SM scheme offers the possibility of electronically capturing both the amplitude and phase of the scattered field. This self-homodyne detection capability has been exploited to spatially map the complex THz permittivity of samples in far-field imaging[28] and more recently in THz-s-SNOM.[29] In the latter case, the amplitude and phase of the scattered field were resolved through mechanical extension of the optical beam path in a manner analogous to interferometric s-SNOM techniques employed at visible and infrared wavelengths.[20,30] However, in contrast to standard interferometric s-SNOM approaches in which a controlled phase delay can be introduced to the scattered beam path, the phase-

resolved LFI scheme requires a phase perturbation be imposed on both incident and scattered beams. In the case of mechanical scanning approaches this unavoidably results in optical misalignment and beam walk-off, which can be particularly problematic both for maintaining the incident beam focus at the nanometric tip and reinjection of the scattered beam to the laser cavity. Ultimately such considerations impose an upper limit on the phase delay, and hence the achievable phase resolution. Moreover, the reliance on mechanical scanning imposes a limit on the acquisition rate, despite the inherently fast (~ps) optical feedback response in THz QCLs.[31] Indeed, fast electronic modulation schemes based on SM in THz QCLs have been demonstrated not only to enable faster acquisition in far-field imaging, but also to significantly improve phase stability owing to the associated reduction in slow thermal drift of the laser emission frequency.[32]

In this work we report *all-electronic* coherent THz-s-SNOM exploiting the SM effect in a QCL. We apply our technique to coherent microscopy of a phonon-resonant crystal and demonstrate spatial mapping of both the amplitude and phase of the scattered field with deeply sub-wavelength resolution. The extracted amplitude and phase parameters reveal clear contrast when compared to both metallic and non-resonant dielectric materials, and show excellent agreement with those calculated using a finite-dipole model of the near-field interaction between the s-SNOM tip and the resonant sample in the Reststrahlen band.

In our experiment a QCL incorporating a photonic lattice on the waveguide ridge was used as the laser source (see Methods and Figure 1). This laser provided single mode emission at ~3.44 THz that could be tuned continuously over a frequency range of ~1 GHz through control of the driving current. The p-polarised radiation emitted from the laser was collected and focused to the $R\sim$25 nm apex of a scanning near-field microscope probe positioned in the near-field of the sample surface. In the s-SNOM arrangement the THz field is strongly confined at the tip apex and after interaction with the sample is scattered to the far-field. In our system this scattered field was coupled back to the QCL along the same optical path as the incident beam and reinjected to the laser cavity. The resulting SM signal was monitored through the QCL terminal voltage and demodulated at the n=1–5 harmonics of the tip tapping frequency ($\Omega\sim$60 kHz) using a lock-in amplifier. By raster scanning the sample two dimensional images revealing the local dielectric properties of the sample in the near-field of the tip were obtained. Measurements performed using a gold-on-dielectric test sample revealed an imaging resolution ~125 nm, commensurate with the radius of the tip apex (see Supporting Information, Figure S1).

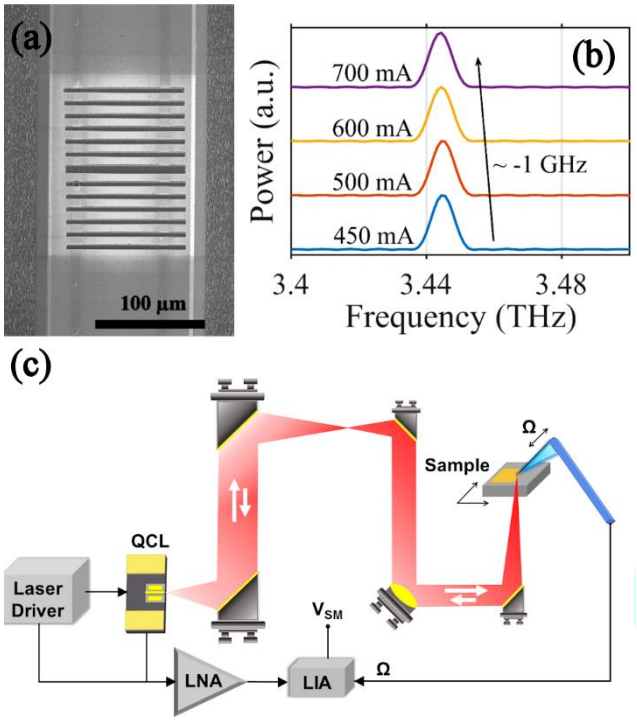

Figure 1. (a) Scanning electron microscope image of the THz QCL device incorporating a finite-site photonic lattice etched in the waveguide ridge. (b) Emission spectra of the QCL obtained at different driving currents, showing emission on a single longitudinal mode that tunes electronically over ~1 GHz. (c) Experimental diagram of coherent THz-s-SNOM system in which radiation from the QCL is coupled to and from the tip of an AFM probe. LIA–Lock-in amplifier; LNA–Low-noise amplifier.

To enable simultaneous measurement of both the amplitude and phase of the scattered field, and thereby capture fully, the coherent near-field interaction between tip and sample, images were acquired with the lasing frequency being tuned by ~−17 MHz between successive raster scans of the sample. For each sampling position (x, y) the frequency-controlled variation of round-trip phase in the external cavity of length L_{ext} formed between laser facet and tip induces a series of interferometric fringes in the SM voltage given by (see Supporting Information):

$$V_{\text{SM}}(x, y) \propto s_n \cos\left(\frac{4\pi L_{\text{ext}} \nu_i}{c} - \phi_n\right) \tag{1}$$

Here s_n and ϕ_n represent the amplitude and phase of the fringes encoded within the n^{th} harmonic of the voltage signal, c is the speed of light, and the lasing frequency under feedback for each frequency step in the multi-spectral image, ν_i, is related to the frequency of the solitary laser through the transcendental excess phase equation. Inherent to this description is the assumption that the modulation amplitude $A_t \ll c/\nu_i$, which is satisfied at THz frequencies even for large tapping amplitudes exceeding ~1

μm. The laser response described by Equation 1 is closely related to that underpinning far-field coherent imaging, in which the amplitude, phase and shape of the SM interferograms recorded under optical feedback from a reflective target encapsulate the complex permittivity of the target material. In the near-field regime the signal parameters instead relate directly to the complex scattering efficiency of the modulated s-SNOM probe in the near-field of the sample, which in turn is dependent on the sample permittivity (see Supporting Information).[29]

Coherent microscopy was demonstrated initially using a target comprising metallic features lithographically patterned on a SiO_2 dielectric substrate (see Methods). Figure 2 shows a series of multi-spectral images recorded from the *n*=3 harmonic signal with laser driving currents in the range I_i = 562−588 mA, corresponding to 14 equally spaced unperturbed emission frequencies spanning ~-220 MHz around ~3.44 THz. Clear contrast between metallic and dielectric regions is observed, with the SM signal in each region swinging between positive and negative voltages in accordance with Equation 1, and attaining maximum (minimum) values when the round-trip phase equals even (odd) multiples of π. The interferometric fringes obtained from a series of images acquired with driving currents in the range I_i = 554−604 mA (corresponding to a frequency span ~-415 MHz) are shown in Figure 3. Here the SM voltages for gold and SiO_2 regions of the sample have been obtained by averaging the voltage signals recorded over representative regions of adjacent pixels from each acquired image. Also shown in this figure are fits to Equation 1 in which the amplitude s_3 and phase ϕ_3 are treated as free parameters. The amplitudes in turn are proportional to the feedback parameter C, which is also treated as a free parameter through the excess phase equation (see Supporting Information). The variation between the fitted curve and measured values in this figure is attributed in part to frequency drift of the laser between scans, arising from drift in the operating temperature. From these fits we obtain experimental values for the ratio of fringe amplitudes, $s_{\mathrm{Au}}/s_{\mathrm{SiO_2}} = 8.4$, and phase contrast $\phi_{\mathrm{Au}} - \phi_{\mathrm{SiO_2}} = +5.0°$, along with the feedback parameters $C = 0.03$ and 0.24 for SiO_2 and gold, respectively.

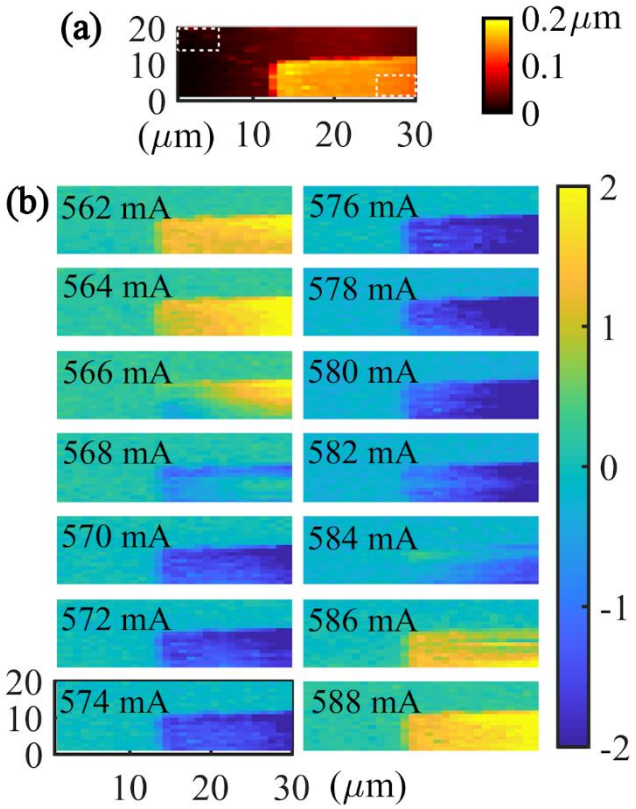

Figure 2. (a) Atomic force microscope image and (b)THz-s-SNOM images of a Au/SiO_2 sample acquired at different laser driving currents, corresponding to a frequency tuning range ~-220 MHz. The image size is 30 μm × 20μm with a pixel size 1 μm × 1 μm, and the acquisition time is ~120 s for each image. The colour scale in (b) depicts the demodulated SM voltage signal recorded at each pixel. The dashed boxes in (a) indicate the areas used to obtain the average voltage signals for Au and SiO_2 regions.

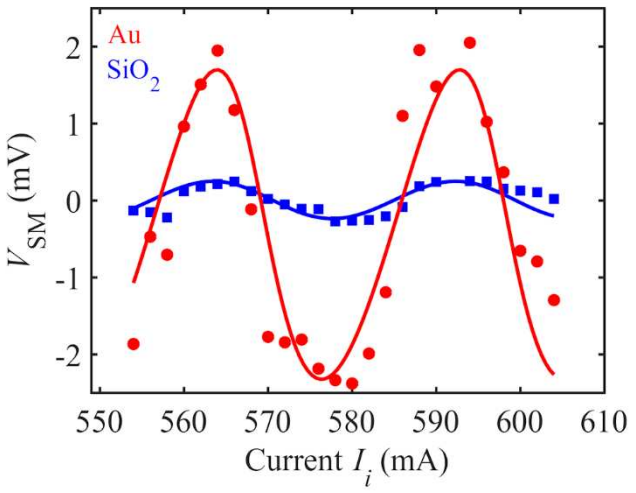

Figure 3. Self-mixing voltages V_{SM} extracted from the series of THz-s-SNOM images shown in Figure 2, for gold (red circles) and SiO_2 (blue squares) regions of the sample.

The solid lines show fits of the data to Equation 1, from which the amplitude and phase parameters of the interferometric fringes are determined.

To elucidate the origin of image contrast in coherent s-SNOM images, we have applied a finite-dipole model to describe the near-field interaction between the tip and sample surface.[33,34] This analytical model treats the tip as an isolated conducting spheroid whose apex is positioned close to a dielectric surface of permittivity ε_s, and which is illuminated by a p-polarised plane wave E_i. The radiation scattered to the far-field from the modulated tip is given by $E_s(t) = E_i s(t) e^{i\phi(t)}$ where $s(t)$ and $\phi(t)$ are the time-dependent magnitude and phase of the complex scattering efficiency, respectively. Noting that the optical feedback coupling strength is proportional to this scattering efficiency it can be shown that the modulated SM voltage signal relates directly to $s(t)$ and $\phi(t)$.[29] By decomposing the scattered far-field into a series of harmonics of the tip modulation frequency we thereby obtain a quantitative description of how the amplitude and phase of the SM fringes, s_n and ϕ_n, are dependent on the sample permittivity (see Supporting Information). In the case of gold and SiO_2 the finite dipole model predicts contrast values $s_{\mathrm{Au}}/s_{\mathrm{SiO_2}} = 9.0$ and $\phi_{\mathrm{Au}} - \phi_{\mathrm{SiO_2}} = +7.0°$, in excellent agreement with the experimentally obtained results. Indeed, near-zero phase parameters are expected for these non-resonant materials, with image contrast arising almost entirely from spatial variation of the scattering amplitude. It should be noted that the small but non-zero phase contrast predicted and measured here arises primarily from the finite conductivity and radiation resistance of the metallic tip rather than through the inherent optical response of the sample.

In order to demonstrate the measurement of phase contrast arising from material properties of the sample, a polar KBr crystal exhibiting a phonon resonance at THz frequencies was studied. Figure 4 shows the complex permittivity of KBr calculated using a single phonon oscillator model (see Supporting Information), along with the corresponding spectral variation of the scattering amplitude and phase, s_3 and ϕ_3, calculated using the finite dipole model. The amplitude and phase calculated for gold are also shown for comparison. As can be seen, in the Reststrahlen band of KBr spanning from ~3.4−4.6 THz the scattered field is characterised by a large phase shift relative to the incident field, whereas the scattering amplitude attains a value comparable to that expected for a metallic sample. At the imaging frequency of ~3.44 THz contrast values $s_{\mathrm{Au}}/s_{\mathrm{KBr}}$ =1.4 and $\phi_{\mathrm{Au}} - \phi_{\mathrm{KBr}}$ =-25° are predicted.

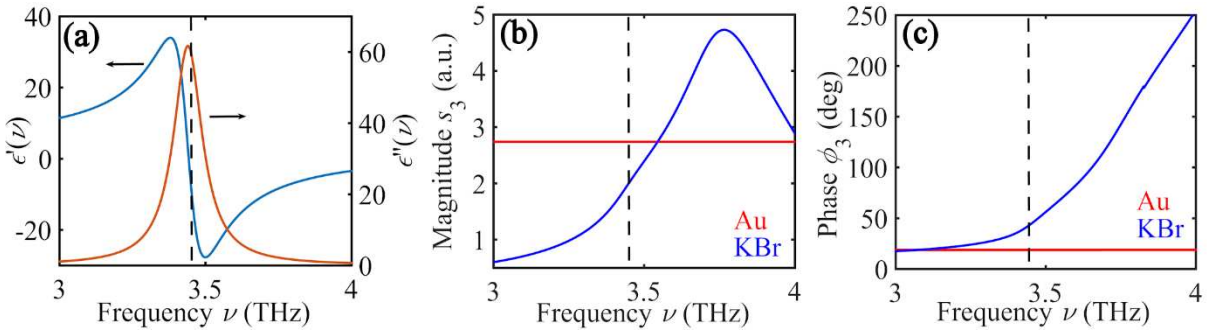

Figure 4. (a) Real $\varepsilon'(\nu)$ (blue, left axis) and imaginary $\varepsilon''(\nu)$ (red, right axis) components of the complex permittivity of KBr determined from a single phonon oscillator model. (b) Magnitude and (c) phase (relative to the excitation field) of the complex scattering efficiency obtained for KBr (blue lines) using the finite dipole model with the sample permittivity shown in (a). Also shown in (b) and (c) are the amplitude and phase calculated for gold (red lines). The vertical dashed line indicates the imaging frequency lying within the Reststrahlen band of KBr.

The interferometric fringes obtained experimentally for these materials are shown in Figure 5, along with fits of the data to the SM model described by Equation 1. The asymmetry of the fringes observed here arises from the larger feedback parameter attained in measurement of these highly-reflective samples, coupled with the non-zero linewidth enhancement factor of the laser, α_{LEF} =2.2, which was determined from the fitting procedure. Although values of α_{LEF} in the range ~−0.1 to ~0.5 are typically obtained for THz QCLs based on a bound-to-continuum active region, we note that values deviating significantly from this range have been reported elsewhere[29,35] for active regions with phonon-assisted electron injection, such as that employed here. A larger magnitude of α_{LEF} may also arise from the photonic lattice that acts as a feedback element in our laser device, such that lasing occurs at frequencies below the peak of the gain profile of the active region where a small α_{LEF} is typically expected. From the fits shown in Figure 5 the contrast values $s_{\mathrm{Au}}/s_{\mathrm{KBr}}$ =0.9 and $\phi_{\mathrm{Au}} - \phi_{\mathrm{KBr}}$ = -35° are obtained. In both cases these are in good agreement with the theoretical expectations, which again exemplifies the ability of our experimental approach to probe coherently the complex permittivity of materials. The discrepancy could originate from the limitations of the electrostatic finite dipole model used here, which may adversely influence our theoretical expectations of the amplitude and phase contrast. In particular, this model does not account for the true geometry of the near-field probe nor the excitation of antenna modes in the probe that are known to significantly influence the scattered field.[36] Such effects are further compounded through dielectric loading of the antenna response by resonant samples such as that investigated in our work. The discrepancies could also originate from variations in the frequency tuning coefficient of the QCL across the operating range.[37] Such nonlinearities are not considered in the fringe fitting procedure and could influence the phase extracted from the experimental data. Nevertheless, with a full and high-

resolution spectral characterisation of the QCL source the precise spectral behaviour could be readily incorporated in our model of the SM voltage signal.

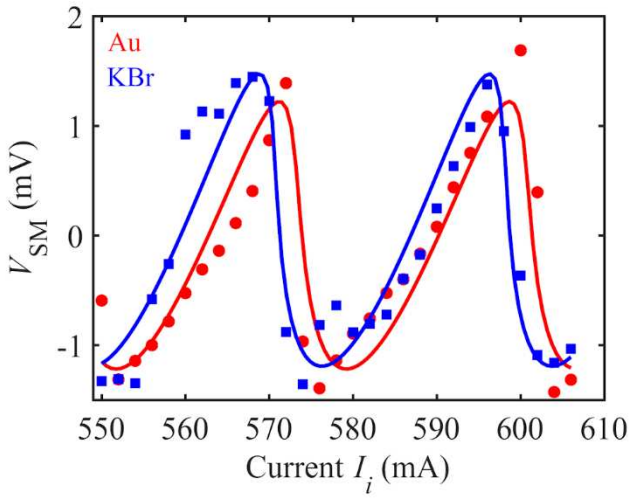

Figure 5. Interferometric fringes obtained for gold (red circles) and KBr (blue squares) regions of a Au/KBr sample, showing phase contrast arising from the TO phonon mode of KBr in the THz frequency band. The solid lines show fits of the data to Equation 1.

In summary we have demonstrated all-electronic coherent scattering-type scanning near-field microscopy using a THz-frequency quantum cascade laser. By exploiting the coherent self-mixing effect in these lasers we are able to resolve both the amplitude and phase of the field scattered from the s-SNOM tip without reliance on slow mechanical scanning approaches to capture the interferometric data. We have applied our technique to coherent microscopy of a phonon-resonant crystal, allowing spatial mapping of the complex scattering efficiency with deeply sub-wavelength resolution. The measured amplitude and phase parameters have been shown to agree with those predicted using a finite-dipole model of the near-field interaction between the tip and sample that incorporates the complex permittivity of the crystal in the Reststrahlen band.

The acquisition rate in our system is currently limited by integration of the small ~µV signal arising from the weak field scattered from the nanometric probe with radius R~25 nm. Nevertheless, since the scattered field is expected to scale approximately as $\propto R^2$ we envisage significantly larger scattered fields could be achieved, albeit at the expense of imaging resolution, with broader probe tips. Specifically, a tip radius R~500 nm would permit a ~400-times reduction in integration time, opening up the possibility of implementing a fast frequency sweep of the laser.[28] Alternatively, larger signals could be accomplished through the use of resonant antenna probes such as those developed for MIR frequencies,[38] or through the use of THz QCLs offering enhanced self-mixing voltage signals.[39]

In addition to offering reduced experimental complexity our approach is not susceptible to optical misalignment and beam walk-off, which can limit the phase delay introduced through mechanical scanning approaches. In this respect we note that the use of THz QCLs offering up to ~21 GHz continuous frequency tuning[40] would permit the acquisition of >80 interferometric fringes in our system. QCLs providing broadly tuneable emission[41] could also be readily implemented in our system, enabling the spectral variation of sample permittivity to be measured across the THz range. We also note this could permit the determination of absolute optical constants of samples through the use of appropriate calibration techniques.[42] Our technique thereby opens the way for fast nanoscale-resolved mapping of the dielectric function of solid state systems and optoelectronic nanodevices at THz frequencies, with applicability to the non-invasive mapping of local strain, conductivity and doping concentrations.[21,43] Our coherent near-field approach is also suited to probing the localised surface fields supported by individual micro-resonators, THz metamaterials and metasurfaces, thereby paving the way for the future design and optimisation of novel THz optoelectronic devices based on these subwavelength structures.[44]

METHODS

Sample fabrication

A 100-nm-thick region of gold was defined on the SiO_2 substrate using standard optical lithography and thermal evaporation. For the KBr substrate, due to its free solubility in water, the region of gold was defined using a mechanical mask formed from Kapton tape.

THz-s-SNOM system

The THz QCL device consisted of a 14-μm-thick GaAs/AlGaAs 9-well active region based on LO-phonon-assisted interminiband transitions, which was processed into a semi-insulating surface-plasmon ridge waveguide with dimensions of 1.8 mm × 150 μm. To achieve lasing on a single longitudinal mode a 166-μm-long finite-site photonic lattice was patterned through the top contact layers using focussed-ion beam milling.[37] The lattice period was 13.2 μm with a 70% mark-space ratio and a central 8-μm-wide phase defect. Emission spectra of the device were measured using a Fourier transform infrared spectrometer with spatial resolution 7.5 GHz.

The QCL was cooled using a continuous-flow L-He cryostat and maintained at a heat sink temperature of 20 ± 0.01 K. A dc current source was used to drive the laser with the SM signal derived from the laser terminal voltage following ×2000 amplification using an ac-coupled low-noise voltage amplifier. The length of the external cavity formed between the s-SNOM tip and the QCL facet was $L_{\mathrm{ext}} = 60$ cm. The s-SNOM system was a commercial neaSNOM system (neaspec GmbH) equipped with a high-frequency Pt probe (25Pt200B-H from Rocky Mountain Nanotechnology). For measurements of the SiO_2/Au sample a tip tapping amplitude of 25 nm and an integration time of 200 ms per pixel were used. For the KBr/Au sample an amplitude

~160 nm and 300 ms integration time were used. Measurements were performed in an unpurged atmosphere with relative humidity ~50%.

ASSOCIATED CONTENT

Supporting Information

Further data and details on the experimental system, and further details of the underlying theory and modelling used in this work, described in the following sections: Measurement of spatial resolution; Laser response to optical feedback; Finite dipole modelling of scattering from tip. This material is available free of charge via the internet at http://pubs.acs.org.

AUTHOR INFORMATION

Corresponding Author

* p.dean@leeds.ac.uk

Author Contributions

P.D. conceived the idea. P.R., J.K., N.S. and P.D. developed the experimental set-up and performed the measurements. Samples were fabricated by P.R. under the supervision of M.C.R. Data was analysed by P.R. and J.K. with support from P.D., J.C. and A.D.B. The QCL structure was grown by L.L. under the supervision of E.H.L. Devices were processed by P.R. and I.K. under the supervision of E.H.L and A.G.D. The manuscript was written by P.D., P.R. and N.S. with contributions from all authors.

ACKNOWLEDGMENT

The authors acknowledge support from the EPSRC programme grant 'HyperTerahertz' (EP/P021859/1). ADB acknowledges support from his EPSRC fellowship (EP/P007449/1). EHL acknowledges support from the Royal Society and the Wolfson Foundation.

REFERENCES

1. Baxter, J. B. & Guglietta, G. W. Terahertz Spectroscopy. *Anal. Chem.* **83**, 4342–4368 (2011).
2. Tonouchi, M. Cutting-edge terahertz technology. *Nat. Photonics* **1**, 97–105

(2007).

3. Davies, A. G., Burnett, A. D., Fan, W., Linfield, E. H. & Cunningham, J. E. Terahertz spectroscopy of explosives and drugs. *Mater. Today* **11**, 18–26 (2008).
4. Huber, R. *et al.* How many-particle interactions develop after ultrafast excitation of an electron–hole plasma. *Nature* **414**, 286–289 (2001).
5. Ulbricht, R., Hendry, E., Shan, J., Heinz, T. F. & Bonn, M. Carrier dynamics in semiconductors studied with time-resolved terahertz spectroscopy. *Rev. Mod. Phys*. **83**, 543 (2011).
6. van Loon, M. A. W. *et al.* Giant multiphoton absorption for THz resonances in silicon hydrogenic donors. *Nat. Photonics* **12**, 179–184 (2018).
7. Matsunaga, R. *et al.* Higgs Amplitude Mode in the BCS Superconductors $Nb_{1-x}Ti_xN$ Induced by Terahertz Pulse Excitation. *Phys. Rev. Lett.* **111**, 57002 (2013).
8. Yang, X. *et al.* Lightwave-driven gapless superconductivity and forbidden quantum beats by terahertz symmetry breaking. *Nat. Photonics* **13**, 707–713 (2019).
9. Katayama, I. *et al.* Ferroelectric Soft Mode in a $SrTiO_3$ Thin Film Impulsively Driven to the Anharmonic Regime Using Intense Picosecond Terahertz Pulses. *Phys. Rev. Lett.* **108**, 97401 (2012).
10. Seifert, T. S. *et al.* Femtosecond formation dynamics of the spin Seebeck effect revealed by terahertz spectroscopy. *Nat. Commun.* **9**, 2899 (2018).
11. Sun, Q., He, Y., Liu, K., Fan, S., Parrott, E. P. J., & Pickwell-MacPherson, E. Recent advances in terahertz technology for biomedical applications, *Quant. Imaging Med. Surg.* **7**, 345−355 (2017)
12. Son, J.-H. Terahertz electromagnetic interactions with biological matter and their applications. *J. Appl. Phys.* **105**, 102033 (2009).
13. Zhong, Z., Gabor, N. M., Sharping, J. E., Gaeta, A. L. & McEuen, P. L. Terahertz time-domain measurement of ballistic electron resonance in a single-walled carbon nanotube. *Nat. Nanotechnol.* **3**, 201–205 (2008).
14. Eisele, M. *et al.* Ultrafast multi-terahertz nano-spectroscopy with sub-cycle temporal resolution. *Nat. Photonics* **8**, 841–845 (2014).
15. Günter, G. *et al.* Sub-cycle switch-on of ultrastrong light–matter interaction. *Nature* **458**, 178–181 (2009).
16. Di Pietro, P. *et al.* Observation of Dirac plasmons in a topological insulator. *Nat. Nanotechnol.* **8**, 556–560 (2013).
17. Luo, L. *et al.* Ultrafast manipulation of topologically enhanced surface transport driven by mid-infrared and terahertz pulses in Bi2Se3. *Nat. Commun.* **10**, 607 (2019).
18. Alonso-González, P. *et al.* Acoustic terahertz graphene plasmons revealed by photocurrent nanoscopy. *Nat. Nanotechnol.* **12**, 31–35 (2017).
19. Knoll, B. & Keilmann, F. Near-field probing of vibrational absorption for chemical microscopy . *Nature* **399**, 134–137 (1999).

20. Zenhausern, F., Martin, Y. & Wickramasinghe, H. K. Scanning Interferometric Apertureless Microscopy: Optical Imaging at 10 Angstrom Resolution. *Science (80-.).* **269**, 1083 LP – 1085 (1995).

21. Liewald, C. *et al.* All-electronic terahertz nanoscopy. *Optica* **5**, 159–163 (2018).

22. Huber, A. J., Keilmann, F., Wittborn, J., Aizpurua, J. & Hillenbrand, R. Terahertz Near-Field Nanoscopy of Mobile Carriers in Single Semiconductor Nanodevices. *Nano Lett.* **8**, 3766–3770 (2008).

23. Jacob, R. *et al.* Intersublevel Spectroscopy on Single InAs-Quantum Dots by Terahertz Near-Field Microscopy. *Nano Lett.* **12**, 4336–4340 (2012).

24. Acuna, G. *et al.* Surface plasmons in terahertz metamaterials. *Opt. Express* **16**, 18745–18751 (2008).

25. Degl'Innocenti, R. *et al.* Terahertz Nanoscopy of Plasmonic Resonances with a Quantum Cascade Laser. *ACS Photonics* **4**, 2150–2157 (2017).

26. Dean, P. *et al.* Apertureless near-field terahertz imaging using the self-mixing effect in a quantum cascade laser. *Appl. Phys. Lett.* **108**, 91113 (2016).

27. Keeley, J. *et al.* Detection sensitivity of laser feedback interferometry using a terahertz quantum cascade laser. *Opt. Lett.* **44**, 3314–3317 (2019).

28. Rakić, A. D. *et al.* Swept-frequency feedback interferometry using terahertz frequency QCLs: a method for imaging and materials analysis. *Opt. Express* **21**, 22194 (2013).

29. Giordano, M. C. *et al.* Phase-resolved terahertz self-detection near-field microscopy. *Opt. Express* **26**, 18423–18435 (2018).

30. Lu, Y.-H. *et al.* Infrared Nanospectroscopy at the Graphene–Electrolyte Interface. *Nano Lett.* **19**, 5388–5393 (2019).

31. Gellie, P. *et al.* Injection-locking of terahertz quantum cascade lasers up to 35GHz using RF amplitude modulation. *Opt. Express* **18**, 20799–20816 (2010).

32. Keeley, J. *et al.* Three-dimensional terahertz imaging using swept-frequency feedback interferometry with a quantum cascade laser. *Opt. Lett.* **40**, 994–997 (2015).

33. Cvitkovic, A., Ocelic, N. & Hillenbrand, R. Analytical model for quantitative prediction of material contrasts in scattering-type near-field optical microscopy. *Opt. Express* **15**, 8550–8565 (2007).

34. Amarie, S. & Keilmann, F. Broadband-infrared assessment of phonon resonance in scattering-type near-field microscopy. *Phys. Rev. B* **83**, 45404 (2011).

35. Wienold, M. *et al.* Real-time terahertz imaging through self-mixing in a quantum-cascade laser. *Appl. Phys. Lett.* **109**, 11102 (2016).

36. McLeod, A. S. *et al.* Model for quantitative tip-enhanced spectroscopy and the extraction of nanoscale-resolved optical constants. *Phys. Rev. B* **90**, 85136 (2014).

37. Kundu, I. *et al.* Frequency Tunability and Spectral Control in Terahertz Quantum Cascade Lasers With Phase-Adjusted Finite-Defect-Site Photonic

Lattices. *IEEE Trans. Terahertz Sci. Technol.* **7**, 360–367 (2017).

38. Huth, F. *et al.* Resonant Antenna Probes for Tip-Enhanced Infrared Near-Field Microscopy. *Nano Lett.* **13**, 1065–1072 (2013).
39. Grier, A *et al.* Origin of terminal voltage variations due to self-mixing in terahertz frequency quantum cascade lasers. Optics Express **24**, 21948–21956 (2016).
40. Kundu, I. *et al.* Wideband Electrically Controlled Vernier Frequency Tunable Terahertz Quantum Cascade Laser. *ACS Photonics* **7**, 765–773 (2020).
41. Khanna, S. P., Salih, M., Dean, P., Davies, A. G. & Linfield, E. H. Electrically tunable terahertz quantum-cascade laser with a heterogeneous active region. Appl. Phys. Lett. 95, 181101 (2009).
42. Guo, X., Bertling, K. & Rakić, A. D. Optical constants from scattering-type scanning near-field optical microscopy. *Appl. Phys. Lett.* **118**, 041103 (2021)
43. Lloyd-Hughes, J. Terahertz spectroscopy of quantum 2D electron systems. *J. Phys. D. Appl. Phys.* **47**, 374006 (2014).
44. Shi, J. *et al.* THz photonics in two dimensional materials and metamaterials: properties, devices and prospects. *J. Mater. Chem. C* **6**, 1291–1306 (2018).

For Table of Contents Use Only

All-electronic phase-resolved THz microscopy using the self-mixing effect in a semiconductor laser

Pierluigi Rubino, James Keeley, Nikollao Sulollari, Andrew D. Burnett, Alex Valavanis, Imon Kundu, Mark C. Rosamond, Lianhe Li, Edmund H. Linfield, A. Giles Davies, John E. Cunningham and Paul Dean